

Scalable native multiqubit gates via engineered noncomputational-state interactions in superconducting fluxonium qubits

Peng Zhao,^{1,*} Peng Xu,^{2,3} and Zheng-Yuan Xue^{4,5,1,†}

¹Quantum Science Center of Guangdong-Hong Kong-Macao Greater Bay Area, Shenzhen 518045, China

²Institute of Quantum Information and Technology, Nanjing University of Posts and Telecommunications, Nanjing, Jiangsu 210003, China

³State Key Laboratory of Quantum Optics Technologies and Devices, Shanxi University, Taiyuan, 030006, China

⁴Key Laboratory of Atomic and Subatomic Structure and Quantum Control (Ministry of Education), Guangdong Basic Research Center of Excellence for Structure and Fundamental Interactions of Matter, and School of Physics, South China Normal University, Guangzhou 510006, China

⁵Guangdong Provincial Key Laboratory of Quantum Engineering and Quantum Materials, Guangdong-Hong Kong Joint Laboratory of Quantum Matter, and Frontier Research Institute for Physics, South China Normal University, Guangzhou 510006, China

(Dated: January 26, 2026)

Native multiqubit gates could be essential for bridging the gap from current noisy devices to future utility-scale quantum computers, as they can substantially reduce circuit depth for near-term applications on noisy devices and may also lower the physical overhead of fault-tolerant quantum computation. Here we introduce a scalable protocol for implementing native multi-controlled gates on fluxonium qubits, supporting an arbitrary number of control qubits ($N > 1$) while remaining compatible with existing single- and two-qubit gate realizations. Our approach leverages engineered interactions in noncomputational state manifolds to enable qubit-state selective transitions, which is activated for the direct implementation of $(C^{\otimes N})Z$ gates. We show that in square lattices with fluxonium qubits, CCZ , $CCCZ$, and $CCCCZ$ gates with errors around 0.01 (0.001) are achievable, with gate lengths of 50 (100) ns, 100 (250) ns, and 150 (300) ns, respectively. Looking forward, integrating these native multi-controlled gates with primitive single- and two-qubit gate sets within a single quantum processor could significantly enhance flexibility in circuit synthesis and offer a promising alternative pathway toward utility-scale quantum computing.

I. INTRODUCTION

Superconducting qubits [1, 2] are a promising platform for quantum computing. Beyond the prevalent transmon qubit [3], fluxonium [4] has emerged as a compelling alternative, demonstrating long coherence times [5–7] and high-fidelity single- and two-qubit gate operations [8–18], benefits enabled by its strong anharmonicity and resilience to dielectric and flux noise [5, 19]. To advance toward utility-scale implementations, the key challenge is now to scale these performance metrics through extensible coupling architectures and control methods [11, 20, 21].

Generally, quantum computing can, in principle, be achieved using only single- and two-qubit gates, as arbitrary gate operations can be decomposed into sequences of these elementary gates [22]. This principle holds across physical platforms, including superconducting qubits. However, many essential quantum algorithms are more naturally expressed through native multi-qubit gates [23–25], whose decomposition into these primitive gates often introduces significant overhead in circuit depth and gate count [26–28] and thus proves inefficient for practical implementation. Consequently, native implementations of multi-qubit operations may offer substantial advantages for both near-term applications [29] and the long-term development of fault-tolerant quantum computing [30–34].

Despite these advantages and various proposed implementations [35–48], the practical implementation and application of native multi-qubit gates in superconducting quantum computing remain scarce [49–57]. Generally, this is due to two key challenges. First, while superconducting qubits intrinsically support multi-qubit interactions [38, 40, 41, 46, 58–61], engineering even two-qubit interactions remains difficult, e.g., even optimized two-qubit gates typically exhibit errors an order of magnitude higher than single-qubit operations, see e.g., Ref. [13]. Extending this to three-qubit or larger gates is significantly more challenging, as evidenced by the modest reported fidelities (typically $< 99\%$ for three-qubit gates) [49–57] and the scarcity of studies on gates involving more than three qubits [49]. These limitations mainly stem from control errors due to the complexity of precise multi-qubit Hamiltonian engineering (e.g., engineering strong three-body interactions while suppressing undesired two-body terms for three-qubit gates) [50, 52–54, 56] and incoherence from longer gate lengths (e.g., typically 250–350 ns for microwave-activated three-qubit gates) [49, 52, 53, 55, 56]. Second, the scalability of these multi-qubit gates to large-scale systems and their compatibility with existing single- and two-qubit gate realizations remain uncertain. These constraints currently restrict the practical utility of native multi-qubit operations and stifle the development of their applications for quantum computing.

Here, we show that engineered interactions in noncomputational manifolds of superconducting fluxonium qubits can enable scalable, native realization of $(C^{\otimes N})Z$ gates. This is achieved by engineering qubit-state-selective transitions into noncomputational manifolds. The large frequency separation between the desired transition and other spurious transitions

*Electronic address: shangniguo@sina.com

†Electronic address: zyxue83@163.com

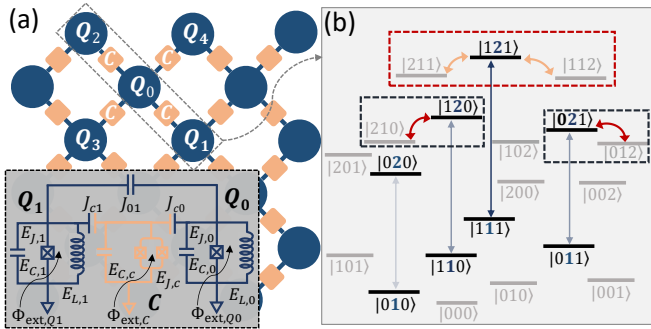


FIG. 1: (a) A 2D square qubit lattice comprising fluxoniums (circles) coupled via couplers (squares). The inset depicts the fluxonium architecture featuring tunable plasmon interactions and qubit-state decoupling, where fluxoniums are coupled via a transmon-based tunable coupler. (b) The energy levels of a three-fluxonium system (with the system-state notation $|Q_1, Q_0, Q_2\rangle$), where Q_0 is coupled to two neighbors Q_1 and Q_2 . The coupler-mediated flip-flop interactions in the noncomputational-state manifolds (curved arrows, $|210\rangle \leftrightarrow |120\rangle$, $|021\rangle \leftrightarrow |012\rangle$, and $|211(112)\rangle \leftrightarrow |121\rangle$) cause neighbor-state-dependent frequency shifts in Q_0 's plasmon transition $|1\rangle \leftrightarrow |2\rangle$ through interaction-induced level repulsions.

allows selective activation of target multi-qubit interactions while suppressing unwanted terms. This approach provides a path beyond existing schemes by enabling fast, scalable native multi-qubit gates without substantially increasing calibration complexity, allowing for their co-integration with primitive single- and two-qubit gates in a unified processor.

II. CIRCUIT MODEL AND SYSTEM HAMILTONIAN

TABLE I: Hamiltonian parameters of the fluxonium system.

	E_C (GHz)	E_L (GHz)	E_J (GHz)
Fluxonium Q_0	1.41	0.80	6.27
Fluxonium Q_1	1.30	0.59	5.71
Fluxonium Q_2	1.33	0.60	5.40
Fluxonium Q_3	1.35	0.63	5.60
Fluxonium Q_4	1.35	0.70	5.60
Transmon C	0.32	–	55
	J_{c0} (MHz)	J_{c1} (MHz)	J_{01} (MHz)
Coupling strengths	500	500	125

For illustration purposes, the fluxonium qubit architecture that we study here is schematically depicted in Fig. 1(a), where fluxonium qubits are arranged in a 2D square lattice with nearest-neighbor coupling mediated by transmon-based tunable couplers (inset). As shown in Ref. [20], these couplers enable both qubit-state decoupling and tunable plasmon interactions. For our theoretical framework (beyond the degree-4 connectivity shown in Fig. 1), we consider a general unit cell of large-scale qubit lattices comprising a central fluxonium Q_0 coupled to N neighboring fluxoniums (Q_1, \dots, Q_N), de-

TABLE II: Qubit parameters and coupler biases of the fluxonium system with the circuit parameters listed in Table I.

	$\omega^{(01)}/2\pi$ (GHz)	$\omega^{(12)}/2\pi$ (GHz)	$\omega^{(03)}/2\pi$ (GHz)
Q_0	0.298	5.621	8.347
Q_1	0.222	5.269	7.461
Q_2	0.273	5.049	7.474
Q_3	0.273	5.198	7.660
Q_4	0.306	5.134	7.771
C	11.537	11.194	–
$(C^{\otimes N})Z$	$N = 1$	$N = 2$	$N = 3$
$\varphi_{\text{ext},cj}/2\pi$	[0.413]	[0.413, 0.420]	[0.403, 0.420, 0.410]

scribed by the Hamiltonian (hereafter, $\hbar = 1$)

$$\begin{aligned}
 H^{(N)} &= \sum_{j=1}^N [H_{0,j}] + H_0 \\
 H_{0,j} &= H_j + [J_{c0}\hat{n}_0\hat{n}_{cj} + J_{cj}\hat{n}_j\hat{n}_{cj} + J_{0j}\hat{n}_0\hat{n}_j] \\
 &\quad + [4E_{C,cj}\hat{n}_{cj}^2 - E_{J,cj}\cos(\frac{\varphi_{\text{ext},cj}}{2})\cos\hat{\varphi}_{cj}]
 \end{aligned} \tag{1}$$

with the fluxonium Hamiltonian $H_k = 4E_{C,k}\hat{n}_k^2 + \frac{E_{L,k}}{2}(\hat{\varphi}_k - \varphi_{\text{ext},k})^2 - E_{J,k}\cos\hat{\varphi}_k$ ($k = 0, j$) [4, 62]. Here, E_C , E_J , and E_L denote the charging, Josephson, and inductive energies, respectively, subscripts j and cj label the fluxonium and the coupler, J_{ck} and J_{0j} represent the coupler-fluxonium and the direct fluxonium-fluxonium coupling strength, and φ_{ext} is the external phase bias with $\varphi_{\text{ext}} = 2\pi\Phi_{\text{ext}}/\Phi_0$. Hereafter, the lowest three energy levels of each fluxonium are denoted by $\{|0\rangle, |1\rangle, |2\rangle\}$ and all fluxoniums are biased at their half-flux quantum sweet spots ($\varphi_{\text{ext},k} = \pi$).

In the present architecture, the small transition dipole of the fluxonium qubit, together with its relatively low qubit transition frequency, enables effective decoupling between the computational subspaces and the couplers, leading to ZZ interactions suppressed below 10 kHz [13, 20]. In contrast, the transmon-like dipole of the fluxonium plasmon transition ($|1\rangle \leftrightarrow |2\rangle$) supports strong coupler-mediated interactions [20]. Thus, here we focus on the plasmon interactions. Assuming that the coupling system operates in the dispersive regime (where the plasmon-coupler detuning significantly exceeds their coupling strength), we can derive an effective Hamiltonian by eliminating the direct fluxonium-coupler coupling terms in Eq. (1) [20]. Projected onto the noncomputational manifold spanned by $\{|1\rangle, |2\rangle\}$, this yields the approximate form (see Appendix A for details)

$$H_{\text{eff}}^{(N)} = \frac{\omega_0^{(12)}}{2} Z_0^{(12)} + \sum_{j=1}^N \left[\frac{\omega_j^{(12)}}{2} Z_j^{(12)} + g_{0j} X_0^{(12)} X_j^{(12)} \right], \tag{2}$$

where $\omega_k^{(12)}$ is the plasmon transition frequency of Q_k , g_{0j} represents the strength of the coupler-mediated flip-flop interaction between Q_0 and Q_j , and $\{X^{(12)} = |1\rangle\langle 2| + |2\rangle\langle 1|, Z^{(12)} = |2\rangle\langle 2| - |1\rangle\langle 1|\}$ are the Pauli operators defined in the $\{|1\rangle, |2\rangle\}$ subspace.

We further consider that the plasmon detuning between Q_0 and its neighbors $\Delta_{0j} = |\omega_0^{(12)} - \omega_j^{(12)}|$ is far larger than the coupling strength g_{0j} , i.e., operating in the dispersive regime, and the N neighboring fluxoniums are non-degenerate in plasmon frequency. This configuration suppresses plasmon excitation exchange among fluxoniums while preserves dispersive interactions between Q_0 and its all neighbors, which make Q_0 's plasmon frequency dependent on the collective state of its neighbors. This dependence becomes explicit when diagonalizing the Hamiltonian in Eq. (2) and keeping only terms involving Q_0 , yielding the approximate form

$$H_{\text{eff},0}^{(N)} = \frac{Z_0^{(12)}}{2} \left(\omega_0^{(12)} + \sum_{\vec{s}} [\delta_{\vec{s}} |\vec{s}\rangle \langle \vec{s}|] \right), \quad (3)$$

where $\delta_{\vec{s}} \equiv \sum_j s_j \chi_j$ is the accumulated frequency shift contributing from all Q_0 's neighbors, which are in state $|\vec{s}\rangle = |s_1, \dots, s_j, \dots, s_N\rangle$ with $s_j = \{0, 1\}$, and $\chi_j \approx g_{0j}^2/\Delta_{0j}$ denotes the dispersive shift from the Q_0 - Q_j interaction.

Equation (3) demonstrates that the dispersive coupling to neighboring fluxoniums generates a state-dependent frequency shift in Q_0 's plasmon transition. This shifts can be engineered for enabling state-selective activation of transitions connecting computational and non-computational subspace and thus inducing non-trivial phase factors for computational states. While such mechanism has been previously exploited for CZ gates in two-qubit systems ($N = 1$) [63, 64], here we generalize this to implement native $(C^{\otimes N})Z$ gates. Since transition selectivity (addressability) is ultimately limited by the shift magnitude, which consequently constrains both gate speed and gate fidelity, we should first analyze the underlying shift mechanism before proceeding to gate implementations, with particular focus on parameter optimization for maximizing the shift and improving the selectivity.

Accordingly, we consider an example of a three-fluxonium system (with the state notation $|Q_1, Q_0, Q_2\rangle$), see Fig. 1(a), where a central fluxonium Q_0 coupled to two neighbors Q_1 and Q_2 ($N = 2$). Figure 1(b) depicts the system energy levels and demonstrates that the level repulsion from the interactions among noncomputational manifolds, i.e., $\{|210\rangle, |120\rangle\}$, $\{|021\rangle, |012\rangle\}$, and $\{|211\rangle, |121\rangle, |112\rangle\}$ (see blue and red dashed boxes), causes the frequency shift in Q_0 's plasmon transition $|1\rangle \leftrightarrow |2\rangle$ (see blue arrows). To be more specific, for two coupled energy levels (e.g., $|210\rangle \leftrightarrow |120\rangle$), the interaction-induced repulsion results in an upward shift of the higher level (e.g., $|120\rangle$) and a downward shift of the lower level (e.g., $|210\rangle$) with the magnitude depending on the coupling strength and the level detuning.

To ensure addressability in these state-dependent transitions, the central fluxonium Q_0 's plasmon frequency can lie either above or below that of all neighbors, see Fig. 1(b) (for the qubit lattice shown in Fig. 1(a), the frequency allocation of fluxonium plasmons in each row and column should follow a zigzag pattern [41]), preventing cancellation of shifts from competing level repulsions with different neighbors. Moreover, while our above analysis assumes the dispersive limit, practical implementations generally need to enter into non-dispersive regimes [65–67] to achieve sufficiently strong shifts

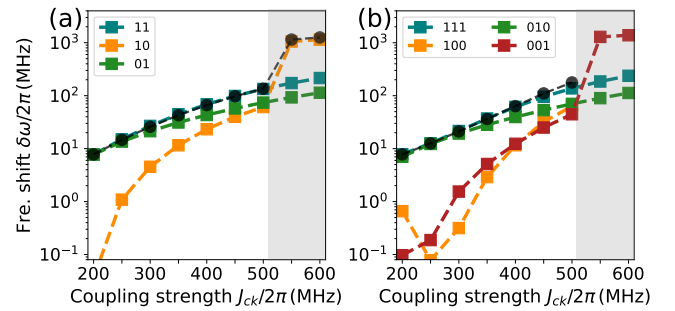


FIG. 2: The neighbor-state-dependent frequency shift in the central fluxonium versus the the coupler-fluxonium coupling strength J_{ck} for $N = 2$ (a) and $N = 3$ (b). Black circles denote the accumulated shift contributing from all neighbors, i.e., $(\delta_{0\vec{1}} + \delta_{\vec{1}0})$ and $(\delta_{00\vec{1}} + \delta_{0\vec{1}0} + \delta_{\vec{1}00})$ are for $N = 2$ and $N = 3$, respectively. The gray regions show the parameter space where the relation of $\delta_{\vec{s}} \equiv \sum_j s_j \chi_j$ breaks down (where the negative values of $\delta_{\vec{1}00}$ are excluded from the data presented in (b)).

for fast gates while maintaining the validity of the approximate model given in Eq. (3) (while the model's validity, in theory, is independent of the number of neighbors, it breaks down for practical large systems, see Appendix B).

To validate the choice of operating regime and the approximate model, we consider the circuit parameters summarized in Table I with the corresponding qubit parameters listed in Table II. Figure 2(a) shows the state-dependent frequency shift versus the coupler-fluxonium coupling strength J_{ck} for $N = 2$ with the coupler biases (for tuning on plasmon interactions) listed in Table II. As J_{ck} increases, the frequency shift grows accordingly. The calculated shift $\delta_{\vec{1}\vec{1}}$ (teal squares) agrees well with the sum of individual neighbor contributions $\delta_{\vec{0}\vec{1}} + \delta_{\vec{1}\vec{0}}$ (black circles) up to $J_{ck}/2\pi \approx 500$ MHz. Beyond this point (gray shaded region), the relationship breaks down and shift magnitudes (e.g., $\delta_{\vec{1}\vec{0}}$ and $\delta_{\vec{1}\vec{0}\vec{0}}$) exhibit abrupt jumps. These behaviors are certainly expected for systems operating far outside the dispersive regime assumed in the derivation of Eqs. (2) and (3). Similar nonlinear effects also appear in the four-qubit case ($N = 3$), see Fig. 2(b), and five-qubit systems ($N = 4$), see Appendix B.

III. MICROWAVE-ACTIVATED $(C^{\otimes N})Z$ GATES

Given the system parameters specified in Table I, here we show that the shifts can enable state-selective transitions in microwave-driven multi-qubit systems, thereby imprinting non-trivial phases on computational states for $(C^{\otimes N})Z$ gate realizations. Figure 3 shows the neighbor-state-dependent plasmon transition frequencies for all fluxoniums (including the central fluxonium) for $N = \{1, 2, 3\}$. As demonstrated in pervious works [13, 63, 64] and also shown in Fig. 3(a) for $N = 1$, large shifts can enable selective driving of one specific transition (i.e., driving the target gate transition while maintaining suppression of all other transitions), e.g., the $|11\rangle \leftrightarrow$

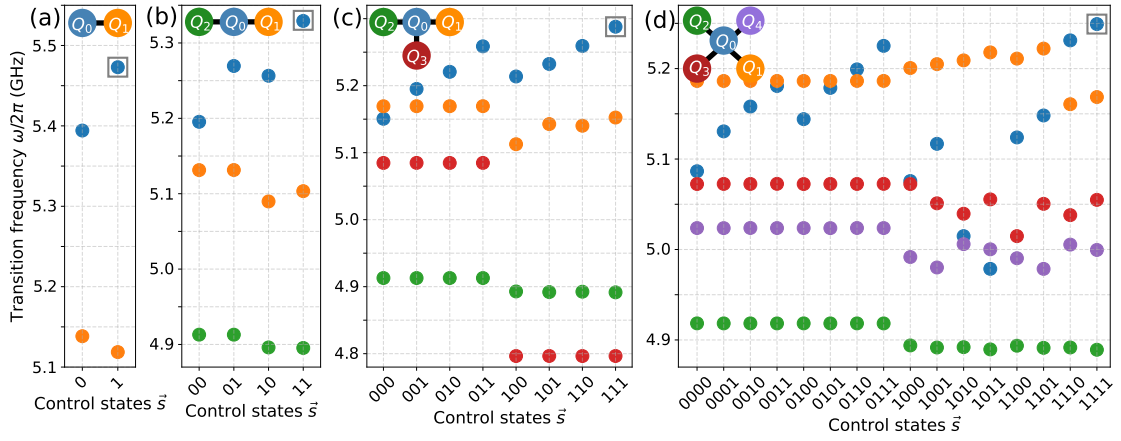


FIG. 3: State-dependent plasmon frequencies for each fluxonium under varying neighbor-state configurations. The gray boxes highlight the gate frequency (i.e., the frequency of the central fluxonium’s $|1\rangle \leftrightarrow |2\rangle$ with all neighbors in state $|1\rangle$) for implementing $(C^{\otimes N})Z$ gates. In (a-d), minimum detunings between the gate transition and other nearby transitions are $(\delta'_{\vec{s}})_{\min}/2\pi = \{-78.8, -59.7, -28.7, -18.0\}$ MHz for $N = \{1, 2, 3, 4\}$, respectively.

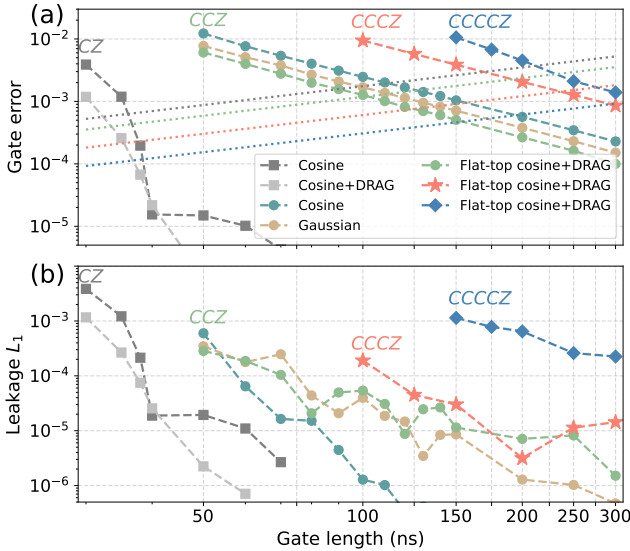


FIG. 4: Gate errors (a) and leakage (b) of $(C^{\otimes N})Z$ ($N = 1, 2, 3, 4$) versus gate lengths (excluding the coupler flux ramping) with different drive pulse shapes. Here, the DRAG pulse parameters are chosen to suppress the spurious transition nearest to the target gate transition, see Fig. 3, and for CCZ , $CCCZ$, and $CCCCZ$ gates, the cosine ramp times of the flat-top pulses are 10 ns, 20 ns, and 30 ns, respectively. In (a), the calculated incoherence gate errors arising from relaxation and dephasing of noncomputational gate levels are represented by dotted lines in distinct colors: gray for CZ , green for CCZ , red for $CCCZ$, and blue for $CCCCZ$ gates.

$|2\rangle$ transition, thus inducing an extra phase accumulation on the $|11\rangle$ state upon completion of a Rabi cycle. A controlled-Z (CZ) gate is thus realized (up to single-qubit Z rotations) when the accumulated phase reaches π . Similarly, as shown

in Figs. 3(b) and 3(c), the shift also enable state-selective plasmon transitions in three- and four-fluxonium systems (as well as five-fluxonium systems, see Fig. 3(d) and Appendix B).

As operating in the non-dispersive regime for fast gates, the system exhibits strong state hybridization within noncomputational manifolds. This generally enables the activation of any computational-to-noncomputational transition with microwave drives applied to any fluxonium in the coupled system, regardless of its site position. The gate speed is thus constrained by the minimal detuning between the target gate transition and all other computational-to-noncomputational transitions, see Fig. 3. We therefore select the central fluxonium Q_0 ’s plasmon transition with the neighbor-state configuration $|1\rangle^{\otimes N}$ (see grey boxes in Fig. 3) as the target transition to maximize gate speed and suppress spurious transitions.

Following Eq. (3), the dynamics with the microwave drive (at the gate transition frequency) on the central fluxonium can be approximately described by the rotating-frame Hamiltonian (with respect to the drive)

$$H_{\text{gate}}^{(N)} = \sum_{|\vec{s}\rangle \neq |1\rangle^{\otimes N}} \left[\left(\frac{\delta'_{\vec{s}}}{2} Z_0^{(12)} + \frac{\Omega}{2} X_0^{(12)} \right) \otimes |\vec{s}\rangle \langle \vec{s}| \right] + \frac{\Omega}{2} X_0^{(12)} \otimes (|1\rangle \langle 1|)^{\otimes N}, \quad (4)$$

where Ω is the drive magnitude and $\delta'_{\vec{s}}$ is the plasmon-drive detuning for Q_0 with the neighbor-state configuration $|\vec{s}\rangle$. From Eq. (4), the drive activates both the target gate transition $|1\rangle \otimes |1, \dots, 1\rangle \leftrightarrow |2\rangle \otimes |1, \dots, 1\rangle$ (the term in the second line) and unwanted off-resonant transitions $|s_0\rangle \otimes |s_1, \dots, 1, \dots, s_N\rangle \leftrightarrow |s_0\rangle \otimes |s_1, \dots, 2, \dots, s_N\rangle$ (the terms in the first line). By choosing the drive length t_g to satisfy $\int_0^{t_g} \Omega dt = 2\pi$ while neglecting these off-resonant transitions, only the computational state $|1\rangle^{\otimes (N+1)}$ acquires a non-trivial phase π , thus implementing the $(C^{\otimes N})Z =$

diag(1, 1, 1, ..., 1, -1) gate up to local Z rotations.

However, in practical implementations, off-resonant transitions can introduce non-negligible errors, particularly when pursuing fast gates through strong drives in systems with many nearby transitions. These spurious transitions primarily generate two error types: leakage and unwanted phase accumulation. While leakage from dominant off-resonance transitions can be mitigated through synchronization protocols [8] or pulse shaping techniques (e.g., DRAG [68]), such methods show limited effectiveness in systems with numerous nearby transitions. The phase, arising from ac-Stark shifts $\sim \Omega^2/4\delta'_s$ due to off-resonant drives, comprise both single-qubit phases (correctable through local Z rotations) and problematic multi-qubit conditional phases. For $(C^{\otimes N})Z$ gates, the off-resonant drives introduce $N + 1$ single-qubit phases and C_{N+1}^n n -qubit conditional phases ($2 \leq n \leq N$). Compensating for the latter typically requires additional multi-qubit phase gates [48, 56] or refocusing techniques [46, 47], undermining the advantages of the native implementations compared to decomposed approaches and also complicating the gate calibration. Thus, here the fundamental strategy for error suppression involves engineering plasmon interactions to maximize the minimal state-dependent detuning $(\delta'_s)_{\text{Min}}$.

Accordingly, in our architecture, $(C^{\otimes N})Z$ gates can be realized by firstly turning on the plasmon interactions (i.e., tuning couplers from their idle points $\varphi_{\text{ext},cj}/2\pi \approx 0$ to the interaction points $\varphi_{\text{ext},cj}/2\pi \approx 0.41$, see Table II) for achieving large $(\delta'_s)_{\text{Min}}$, then applying a resonant 2π -pulse at the gate transition frequency, and finally returning couplers to their idle points. Here, we note that as in Refs. [13, 20, 64], here we employ simultaneous microwave drives with identical amplitude and frequency applied to both Q_0 and Q_1 for realizing target gates and thus reducing unwanted phase accumulations from off-resonant transitions. Following tune-up procedures for CZ gates [13, 20], drive parameters (frequency and peak drive amplitude for a given pulse shape) for CCZ , $CCCZ$, and $CCCCZ$ gates are optimized by minimizing both leakage [69] and target conditional phase errors within the gate subspace, e.g., $\{|1\rangle \otimes |11\rangle, |1\rangle \otimes |01\rangle, |0\rangle \otimes |11\rangle, |0\rangle \otimes |01\rangle\}$ for CCZ gates. We note that the choice of gate subspace remains flexible, with the key essential requirement being that it includes the states involved in the target gate transition. Therefore, for implementing a CCZ gate, an alternative valid gate subspace could be defined as, for example, $\{|1\rangle \otimes |11\rangle, |1\rangle \otimes |01\rangle, |1\rangle \otimes |10\rangle, |1\rangle \otimes |00\rangle\}$.

By considering different pulse shapes (see Appendix C), Figure 4(a) shows $(C^{\otimes N})Z$ gate errors (up to local Z rotations) [70] versus gate lengths (excluding the coupler flux ramping) for $N = \{1, 2, 3, 4\}$ and demonstrates that beyond high-fidelity CZ gates, CCZ , $CCCZ$, and $CCCCZ$ gates with errors of approximately 0.01 (0.001) can also be achieved at gate lengths of 50 (100) ns, 100 (250) ns, and 150 (300) ns, respectively. Furthermore, assuming typical coherence times of $T_1^{21} = T_\phi^{21} = 10 \mu\text{s}$ [8, 13], Figure 4(a) also shows the incoherence gate errors resulting from relaxation and dephasing of non-computational levels during gate operations, see Appendix D. These results indicate that gate errors of ~ 0.001 could be achievable for $N = 2, 3, 4$ un-

der realistic experimental conditions. When further examining the leakage [69] shown in Fig. 4(b), a key difference emerges between CZ and $(C^{\otimes N})Z$ ($N \geq 2$), i.e., while CZ gate performance is predominantly limited by leakage from off-resonant transitions, which can be effectively suppressed using DRAG pulses, $(C^{\otimes N})Z$ ($N \geq 2$) gates are primarily constrained by unwanted conditional phase accumulation, instead of the leakage. As mentioned before, this distinction arises fundamentally because: CZ gates only involves a single two-qubit conditional phase, whereas $(C^{\otimes N})Z$ ($N \geq 2$) gate implementations inherently accumulate unwanted multi-qubit conditional phases (e.g., three, six, and ten two-qubit phases for $N = 2, 3, 4$) through drive-induced ac Stark shifts in addition to the desired multi-qubit phases [71].

IV. CONCLUSION

In conclusion, we propose scalable native multi-qubit $(C^{\otimes N})Z$ gates on fluxonium qubits by exploiting engineered interactions within non-computational state manifolds. We show that microwave-activated, qubit-state-selective transitions facilitate targeted multi-qubit interactions while intrinsically suppressing spurious terms. This mechanism enables fast, high-fidelity gates without a significant increase in calibration complexity. This scalable approach, which combines high performance with simplified tune-up procedures and remains fully compatible with existing single- and two-qubit gates, allows for the integration of native multi-controlled gates with primitive gate sets within a single quantum processor. We anticipate that quantum processors supporting both high-fidelity native multi-qubit gates and primitive gates could benefit both near-term applications, such as algorithm co-design favoring native multi-qubit interactions, and quantum error correction by improving circuit efficiency and reducing overhead.

Acknowledgments

Peng Zhao would like to thank Zhuang Ma, Teng Ma, Meng-Jun Hu, Kunzhe Dai, and Ruixia Wang for insightful discussions, Yanqing Zhu, Xiaotong Ni, Jia Liu, and Lingzhi Tang for their generous support. This work is supported by the National Natural Science Foundation of China (Grants No.12204050 and No.92576110) and the Guangdong Provincial Quantum Science Strategic Initiative (Grant No. GDZX2203001). Peng Xu is supported by the National Natural Science Foundation of China (Grants No.12105146 and No.12175104) and the Program of State Key Laboratory of Quantum Optics Technologies and Devices (No.KF202505).

Appendix A: Effective system Hamiltonian

Following the approach outlined in Ref. [20], here we derive the effective system Hamiltonian presented in the main text. Without loss of generality, we consider the two-qubit

unit cell consisting of a central fluxonium qubit Q_0 coupled to a neighboring fluxonium Q_1 , with their interaction mediated by a transmon-based coupler. The full system Hamiltonian takes the form:

$$H^{(1)} = \sum_{k=0,1} \left[4E_{C,k} \hat{n}_k^2 + \frac{E_{L,k}}{2} (\hat{\varphi}_k - \varphi_{\text{ext},k})^2 - E_{J,k} \cos \hat{\varphi}_k \right] + J_{c0} \hat{n}_0 \hat{n}_{c1} + J_{c1} \hat{n}_1 \hat{n}_{c1} + J_{01} \hat{n}_0 \hat{n}_1 + 4E_{C,c1} \hat{n}_{c1}^2 - E_{J,c1} \cos\left(\frac{\varphi_{\text{ext},c1}}{2}\right) \cos \hat{\varphi}_{c1}. \quad (\text{A1})$$

By approximating the transmon coupler as a weakly anharmonic oscillator [3] and introducing

$$\hat{\varphi}_{c1} = \phi_{c1,\text{zpf}} (\hat{a}_{c1}^\dagger + \hat{a}_{c1}), \quad \hat{n}_{c1} = i n_{c1,\text{zpf}} (\hat{a}_{c1}^\dagger - \hat{a}_{c1}) \quad (\text{A2})$$

with

$$\varphi_{c1,\text{zpf}} = \frac{1}{\sqrt{2}} \left[\frac{8E_{C,c1}}{E_{J,c1}(\varphi_{\text{ext},c1})} \right]^{\frac{1}{4}}, \quad n_{c1,\text{zpf}} = \frac{1}{\sqrt{2}} \left[\frac{E_{J,c1}(\varphi_{\text{ext},c1})}{8E_{C,c1}} \right]^{\frac{1}{4}}, \quad (\text{A3})$$

where a_{c1} (a_{c1}^\dagger) denotes the destroy (creation) operator and $\phi_{c1,\text{zpf}}$ ($n_{c1,\text{zpf}}$) represents the phase (number) zero-point fluctuation, the coupler Hamiltonian can be approximated by

$$H_{\text{coupler}} = \omega_{c1} \hat{a}_{c1}^\dagger \hat{a}_{c1} + \frac{\alpha_{c1}}{2} \hat{a}_{c1}^\dagger \hat{a}_{c1}^\dagger \hat{a}_{c1} \hat{a}_{c1}. \quad (\text{A4})$$

Here, the coupler transition frequency and the coupler anharmonicity are $\omega_{c1} = \omega_{p1}(1 - 3\lambda_1 - 9\lambda_1^2)$ and $\alpha_{c1} = -\omega_{p1}(3\lambda_1 + \frac{162}{8}\lambda_1^2)$ [72], respectively, with

$$\omega_{p1} = \sqrt{8E_{J,c1}(\varphi_{\text{ext},c1})E_{C,c1}}, \quad \lambda_1 = \frac{1}{3} \sqrt{\frac{E_{C,c1}}{8E_{J,c1}(\varphi_{\text{ext},c1})}}. \quad (\text{A5})$$

Focusing on the fluxonium's plasmon transition of $|1\rangle \leftrightarrow |2\rangle$, the system Hamiltonian becomes (redefining $a = -ia$ and $a^\dagger = ia^\dagger$)

$$H_{12}^{(1)} = \sum_{k=0,1} \left[\frac{\omega_k^{(12)}}{2} Z_k^{(12)} + g_{12,k} X_k^{(12)} (\hat{a}_{c1} + \hat{a}_{c1}^\dagger) \right] + H_{\text{coupler}} + g_{12,01} X_0^{(12)} X_1^{(12)}, \quad (\text{A6})$$

where $\{X^{(12)} = |1\rangle\langle 2| + |2\rangle\langle 1|, Z^{(12)} = |2\rangle\langle 2| - |1\rangle\langle 1|\}$ are the Pauli operators defined in the $\{|1\rangle, |2\rangle\}$ subspace, $g_{12,k} \equiv J_{ck} n_{c1,\text{zpf}} \langle 1|n_k|2\rangle$ and $g_{12,01} = J_{01} \langle 1|n_0|2\rangle \langle 1|n_1|2\rangle$ denote the coupling strength of the plasmon-coupler interaction and the direct plasmon-plasmon interaction, respectively.

Considering that the system operates in the dispersive regime, i.e., the interaction strength $g_{12,k}$ significantly smaller than the fluxonium-coupler detuning $\Delta_{12,k} = |\omega_k^{(12)} - \omega_{c1}|$, an effective Hamiltonian (to second order in $g_{12,k}/\Delta_{12,k}$) can be obtained by eliminating the direct plasmon-coupler interactions [73, 74], leading to (recovering the formula shown in

Eq. (2) of the main text with $N = 1$)

$$H_{\text{eff}}^{(1)} = \sum_{k=0,1} \left[\frac{\omega_k^{(12)}}{2} Z_k^{(12)} \right] + g_{01} X_0^{(12)} X_1^{(12)}, \quad (\text{A7})$$

$$g_{01} = g_{12,01} + \frac{g_{12,0}g_{12,1}}{2} \left[\sum_{k=0,1} \left(\frac{1}{\Delta_{12,k}} - \frac{1}{S_{12,k}} \right) \right],$$

with $S_{12,k} = \omega_k^{(12)} + \omega_{c1}$. For clarity, here we omit the renormalization of the plasmon transition frequency due to the plasmon-coupler interactions.

Further assuming that the plasmon-plasmon detuning $\Delta_{01} = |\omega_0^{(12)} - \omega_1^{(12)}|$ is far larger than the plasmon-plasmon coupling strength g_{01} , i.e., Q_0 and Q_1 are coupled dispersively, Equation (A7) can be further simplified by eliminating the plasmon-plasmon coupling term (to second order in g_{01}/Δ_{01}), i.e.,

$$H_{\text{eff}}^{(1)} = \frac{Z_0^{(12)}}{2} (\omega_0^{(12)} + \chi_1) + \frac{Z_1^{(12)}}{2} (\omega_1^{(12)} - \chi_1), \quad (\text{A8})$$

with $\chi_1 = g_{01}^2/\Delta_{01}$ denoting the dispersive shift. Note that the above equation is implicitly defined in the two-fluxonium subspace spanned by $\{|11\rangle, |12\rangle, |21\rangle, |22\rangle\}$. This means that the dispersive shift in one fluxonium's plasmon transition becomes active only when its coupled neighbor is in excited states. Consequently, when restricting to Q_0 and projecting onto Q_1 's computational basis $|0\rangle, |1\rangle$, the dispersive Hamiltonian reduces to:

$$H_{\text{eff},0}^{(1)} = \frac{Z_0^{(12)}}{2} (\omega_0^{(12)} + \chi_1 |1\rangle\langle 1|). \quad (\text{A9})$$

This recovers the formula shown in Eq. (3) of the main text with $N = 1$.

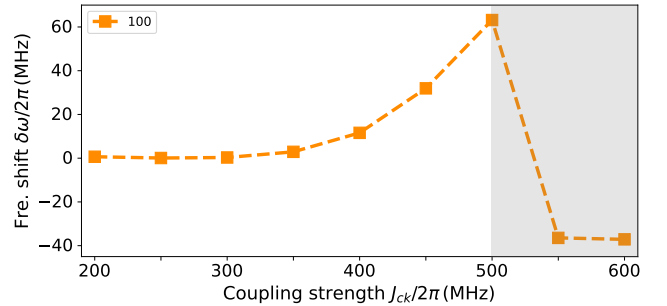


FIG. 5: The neighbor-state-dependent frequency shift δ_{100}^- versus the the coupler-fluxonium coupling strength J_{ck} for $N = 3$. The gray regions show the parameter space where the approximate model breaks down, characterized by δ_{100}^- undergoing discontinuous transitions between positive and negative values. Here the coupler biases are listed in Table II (namely [0.403, 0.420, 0.410]).

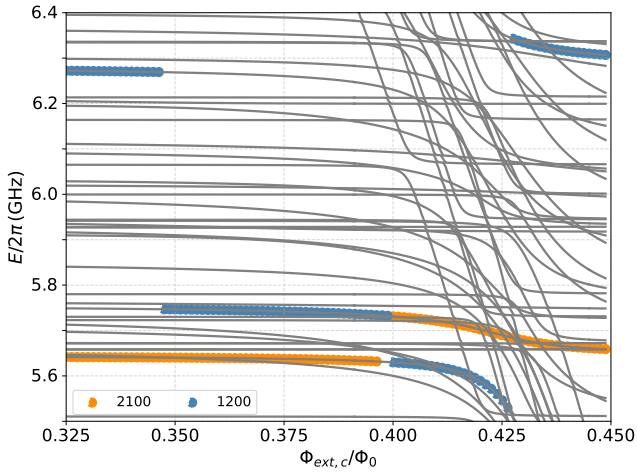


FIG. 6: Energy levels of the four coupled fluxonium system ($N = 3$) versus the coupler flux bias $\varphi_{\text{ext},c3}$. Here, the coupler-fluxonium coupling strength is $J_{ck}/2\pi = 500$ MHz and the other two couplers are biased at $\varphi_{\text{ext},c1(c2)}/2\pi = 0.403$ (0.42).

Appendix B: Extensibility of $(C^{\otimes N})Z$ gate implementations

In theory, the validity of the approximate model is independent of neighbor count, especially for systems operated in the dispersive regime. However, achieving large state-dependent shifts and fast gates typically requires operating in strong non-dispersive regimes, necessitating careful parameter optimization to balance shift magnitude with model validity. For the circuit parameters in Table I, Figure 3 (see the main text) reveals model breakdown (evidenced by the shift magnitude undergoing abrupt jumps) when $J_{ck}/2\pi \geq 500$ MHz for $N = 2, 3$. This is further demonstrated in the four-qubit system ($N = 3$) by the discontinuous sign transitions of $\delta_{100\bar{0}}$ with increasing J_{ck} , see Fig. 5 with the coupler biases listed in Table II (namely [0.403, 0.420, 0.410]). By examining the system spectrum, we find that these discontinuous sign transitions result from on-resonant plasmon coupling between Q_0 and Q_1 . More specifically, Fig. 6 shows the system spectrum as a function of one coupler bias while the other two are fixed at [0.403, 0.420]. Near a coupler bias of about 0.400, a clear avoided crossing appears between the states $|2100\rangle$ and $|1200\rangle$, corresponding precisely to the plasmon coupling between Q_0 and Q_1 .

Analogous discontinuities in frequency shifts also appear in five-qubit systems ($N = 4$, see Fig. 7), where similar level-repulsion-induced collisions occur, as shown in Fig. 8(a). Figure 8(b) shows that such collisions can be partially mitigated by increasing the Q_0 - Q_1 plasmon detuning. We thus expect that level-repulsion induced collisions can be more frequent in larger systems with crowding spectrums.

Moreover, although the approximate model predicts that the magnitude of the minimum state-dependent detuning $(\delta'_{\vec{s}})_{\text{Min}}$ depends solely on the plasmon detuning Δ_k and coupling strengths g_{0k} (independent of neighbor count), one

can expect that practical coupling systems operating in non-dispersive regimes with strong state hybridization should exhibit a clear neighbor-dependent reduction in $(\delta'_{\vec{s}})_{\text{Min}}$. As demonstrated in Figs. 3 and 8(a), the detuning magnitude decreases progressively from -78.8 MHz ($N = 1$) to -18.0 MHz ($N = 4$) with increasing neighbor number. Furthermore, the substantial capacitive coupling required (~ 500 MHz) between fluxoniums and transmon-based couplers introduces significant capacitive loading [13, 75], given the typical ~ 1 GHz charge energies of fluxonium qubits. This physical constraint makes high-connectivity architectures ($N > 4$) based on fluxoniums particularly challenging to implement [75]. Consequently, all these considerations suggest that realizing fast $(C^{\otimes N})Z$ gates for $N > 4$ presents non-trivial engineering challenges that require careful system design.

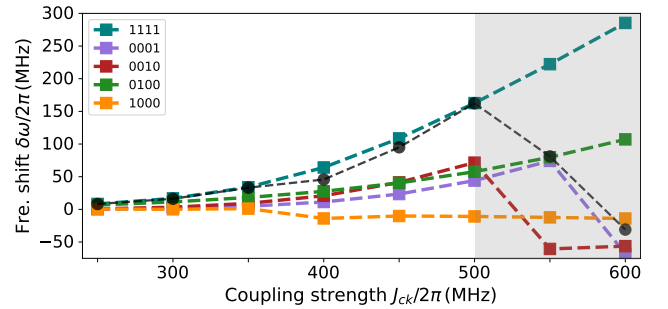


FIG. 7: The neighbor-state-dependent frequency shift in the central fluxonium versus the coupler-fluxonium coupling strength J_{ck} for $N = 4$. Black circles denote the accumulated shift contributing from all neighbors, i.e., $(\delta_{000\bar{1}} + \delta_{001\bar{0}} + \delta_{010\bar{0}} + \delta_{100\bar{0}})$. The gray regions indicate the parameter space where the relation of $\delta_{\vec{s}} \equiv \sum_j s_j \chi_j$ breaks down.

Appendix C: Microwave-activated $(C^{\otimes N})Z$ gates

Following approaches for CZ gate realization [13, 20, 64], here we employ simultaneous microwave drives with identical amplitude and frequency applied to both Q_0 and Q_1 for realizing target gates and reducing unwanted phase accumulations from off-resonant transitions. The corresponding driven Hamiltonian takes the form:

$$H_d = \sum_{k=0,1} A(t) \cos(\omega_d t + \phi_k) \hat{n}_k, \quad (\text{C1})$$

where A , ω_d , and ϕ_k denotes the amplitude, frequency, and the phase of the drive, respectively. Note that the relative phase between the two drives are determined by maximizing constructive interference at the target gate transition [13].

As shown in Fig. 9, we consider using three types of pulses for driving gate transitions, i.e., (i) *Cosine*, which is defined by

$$A(t) = \Omega_d \left(1 - \cos \frac{2\pi t}{t_g} \right), \quad (\text{C2})$$

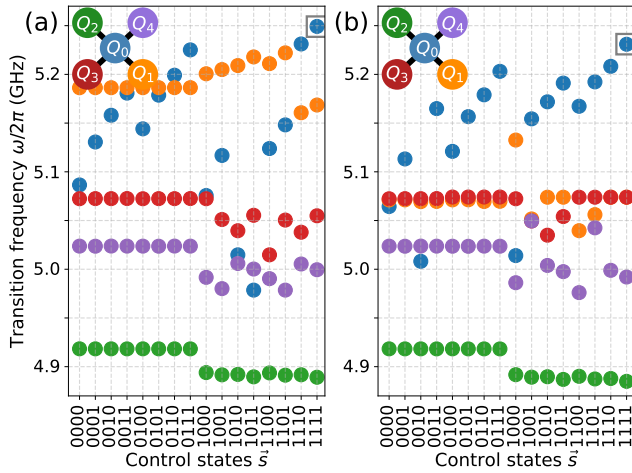


FIG. 8: State-dependent plasmon transition frequencies for each fluxonium under varying neighbor-state configurations with $N = 4$. (a) The gray box highlights the gate frequency for implementing $CCCCZ$ gates with the minimum state-dependent detuning of $(\delta'_{\bar{s}})_{\text{Min}}/2\pi = -18.0$ MHz and the coupler biases at their interaction configurations are $\varphi_{\text{ext},cj}/2\pi = [0.395, 0.419, 0.413, 0.411]$. (b) The circuit parameters are same as in (a), except for Q_1 's E_J , which is adjusted to 5.60 GHz. This modification yields the modified fluxonium transition frequencies $\{\omega_1^{(01)}, \omega_1^{(12)}, \omega_1^{(03)}\}/2\pi = \{0.223, 5.83, 7.422\}$ GHz with increased plasmon detuning between Q_0 and Q_1 . Here, the coupler biases are $\varphi_{\text{ext},cj}/2\pi = [0.410, 0.419, 0.413, 0.411]$, leading to $(\delta'_{\bar{s}})_{\text{Min}}/2\pi = -22.7$ MHz.

where Ω_d denotes the peak drive amplitude and t_g represents the gate length (excluding the coupler bias ramping); (2) *Gaussian*, which has the following form

$$A(t) = \Omega_d \frac{e^{-\frac{(t-t_g/2)^2}{2\sigma^2}} - e^{-\frac{(t_g/2)^2}{2\sigma^2}}}{1 - e^{-\frac{(t_g/2)^2}{2\sigma^2}}}. \quad (\text{C3})$$

with $\sigma = t_g/2$; (iii) *Flat-top cosine*, that is given as

$$A(t) \equiv \begin{cases} \Omega_d \frac{1 - \cos(\pi \frac{t}{t_r})}{2}, & 0 < t < t_r \\ \Omega_d, & t_r < t < t_g - t_r \\ \Omega_d \frac{1 - \cos(\pi \frac{t_g - t}{t_r})}{2}, & t_g - t_r < t < t_g \end{cases} \quad (\text{C4})$$

with the ramp time t_r , and the full DRAG pulse is $A_{\text{DRAG}}(t) = A(t) + i \frac{\alpha}{(\delta'_{\bar{s}})_{\text{Min}}} \dot{A}(t)$ with $\alpha = 1$ for minimizing leading leakage sources. Figures 9(a,d,g) also shows the typical flux pulse for basing the couplers, i.e., tuning the coupler from their idle configurations to the interaction points.

As mentioned in the main text, the gate parameters (i.e., the drive peak amplitude Ω_d and the drive frequency ω_d) are optimized by minimizing both leakage [69] and target conditional phase errors within the gate subspace given as $\{|1\rangle \otimes |11\rangle, |1\rangle \otimes |01\rangle, |0\rangle \otimes |11\rangle, |0\rangle \otimes |01\rangle\}$ for $N = 2$, $\{|1\rangle \otimes |111\rangle, |1\rangle \otimes |011\rangle, |0\rangle \otimes |111\rangle, |0\rangle \otimes |011\rangle\}$ for $N = 3$, and $\{|1\rangle \otimes |1111\rangle, |1\rangle \otimes |0111\rangle, |0\rangle \otimes |1111\rangle, |0\rangle \otimes |0111\rangle\}$

for $N = 4$. Given the optimized gate parameters, Figure 9 shows the typical gate dynamics. Notably, comparisons between implementations without (b,e,h) and with (c,f,i) coupler flux ramping reveal negligible population differences (at the level of $\sim 10^{-4}$). This is consistent with expectations given the near-complete decoupling of the computational subspace and the coupler that effectively suppresses non-adiabatic transitions for computational states during coupler flux ramping [20].

To evaluate the intrinsic gate performance (excluding decoherence effects), we employ the metric of state-average gate fidelity [70]. For $(C^{\otimes N})Z$ gates, the fidelity is calculated following, up to single-qubit Z rotations:

$$F_N = \frac{\text{Tr}(\tilde{U}^\dagger \tilde{U}) + |\text{Tr}(U_i^\dagger \tilde{U})|^2}{n(n+1)}, \quad (\text{C5})$$

where \tilde{U} represents the truncated actual evolution operator within the $n = 2^{N+1}$ -dimensional computational subspace and U_i corresponds to the ideal target gate. Using this framework, we characterize the $(C^{\otimes N})Z$ gate performance as a function of gate length (see Fig. 4 of the main text), with corresponding optimized parameters shown in Fig. 10.

Note that the actual evolution operator \tilde{U} is obtained through numerical simulation of the gate dynamics using the QuTiP package [76], where each fluxonium is truncated to its four lowest energy levels and each transmon coupler is modeled as an anharmonic oscillator (Eq. A4) truncated to three levels. For the $CCCCZ$ gate simulations, we additionally project the full five-fluxonium system Hamiltonian (with a dimension of 82,944) onto a reduced subspace containing states whose energies lie below 24 GHz, yielding a manageable dimension of 6,096 while preserving the essential physics of the fluxonium system.

Appendix D: Gate errors due to relaxation and dephasing of non-computational gate levels

In high-coherence fluxonium systems, as demonstrated in Ref. [13], the dominated incoherence gate error should be from relaxation and dephasing of non-computational gate states. To evaluate these incoherence gate errors, here we thus focus on the gate transition $|1\rangle \otimes |1, \dots, 1\rangle \leftrightarrow |2\rangle \otimes |1, \dots, 1\rangle$. Following the procedure given in Refs. [20, 77], the incoherence gate error from the relaxation and dephasing (white noise) are

$$\begin{aligned} \epsilon_1 = 1 - F_1 &= \frac{3}{32} \frac{t_g}{T_1^{21}} + \frac{13}{80} \frac{t_g}{T_{\phi, \text{white}}^{21}}, \\ \epsilon_2 = 1 - F_2 &= \frac{35}{576} \frac{t_g}{T_1^{21}} + \frac{11}{96} \frac{t_g}{T_{\phi, \text{white}}^{21}}, \\ \epsilon_3 = 1 - F_3 &= \frac{67}{2176} \frac{t_g}{T_1^{21}} + \frac{65}{1088} \frac{t_g}{T_{\phi, \text{white}}^{21}}, \\ \epsilon_4 = 1 - F_4 &= \frac{131}{8448} \frac{t_g}{T_1^{21}} + \frac{43}{1408} \frac{t_g}{T_{\phi, \text{white}}^{21}} \end{aligned} \quad (\text{D1})$$

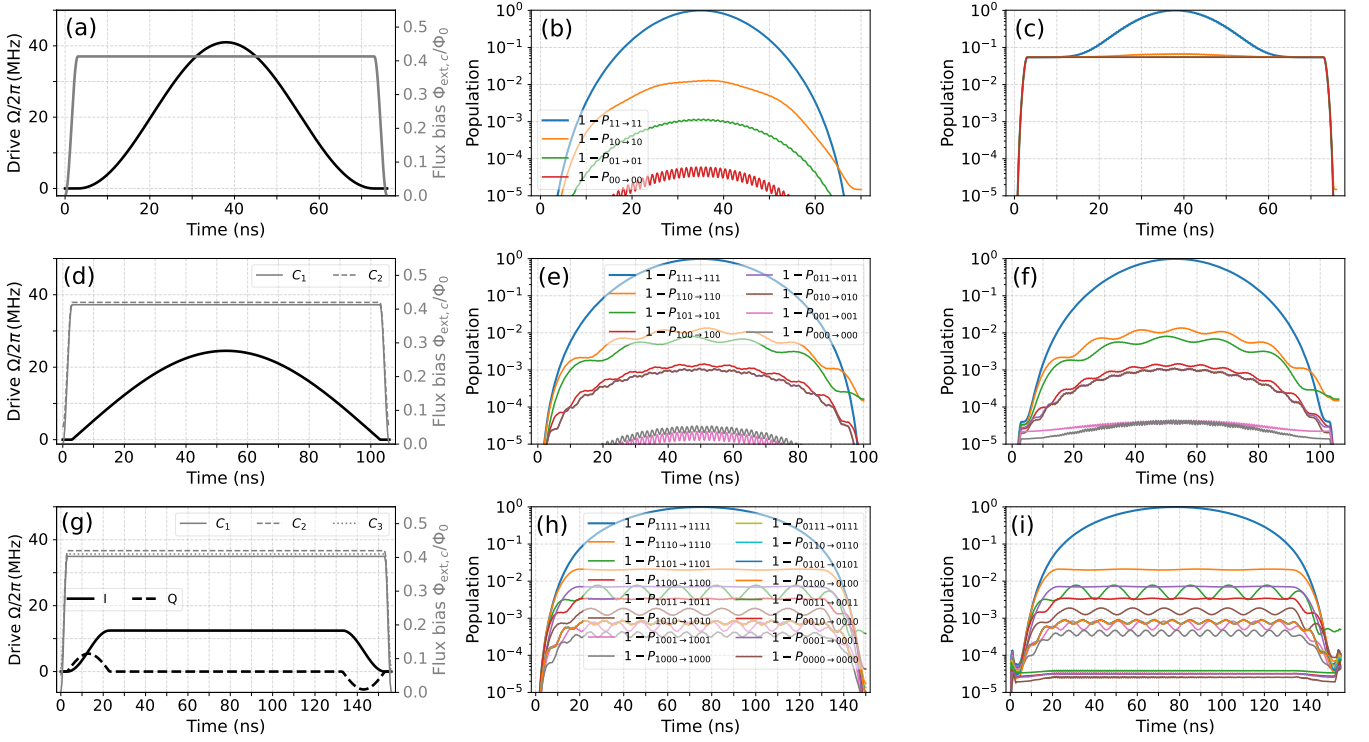
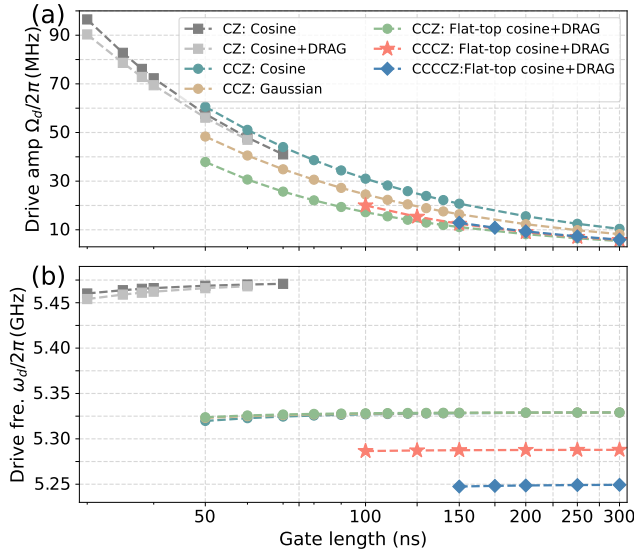


FIG. 9: (a,d,g) Typical control pulse shapes (Cosine, Gaussian, and Flat-top cosine with DRAG correction) alongside (b,c; e,f; h,i) the corresponding gate dynamics for microwave-activated ($C^{\otimes N}$)Z gates, comparing implementations without (b,e,h) and with (c,f,i) coupler flux ramping. In (a,d,g), grey lines denote the flux pulses (flat-top cosine) for biasing the coupler during gates with the ramp time of 3 ns. (a,b,c), (d,e,f), and (g,h,i) are for $N = 1, 2, 3$, respectively. $P_{s \rightarrow s}$ denotes the population in $|s\rangle$ with the system initialized in the state of $|s\rangle$.



for CZ, CCZ, CCCZ, and CCCCZ, respectively, where T_1^{21} and $T_{\phi, \text{white}}^{21}$ denote the relaxation time and the dephasing (white noise) time of the non-computational level $|2\rangle \otimes |1, \dots, 1\rangle$.

FIG. 10: The optimized ($C^{\otimes N}$)Z gate parameters (i.e., gate drive amplitudes and drive frequencies) used for the results shown in Figs. 4 of the main text.

- [1] M. Kjaergaard, M. E. Schwartz, J. Braumüller, P. Krantz, J. I.-J. Wang, S. Gustavsson, and W. D. Oliver, Superconducting qubits: Current state of play, *Annu. Rev. Condens. Matter Phys.* **11**, 369 (2020).
- [2] A. Gyenis, A. D. Paolo, J. Koch, A. Blais, A. A. Houck, and D. I. Schuster, Moving beyond the Transmon: Noise-Protected Superconducting Quantum Circuits, *PRX Quantum* **2**, 030101 (2021).
- [3] J. Koch, T. M. Yu, J. Gambetta, A. A. Houck, D. I. Schuster, J. Majer, A. Blais, M. H. Devoret, S. M. Girvin, and R. J. Schoelkopf, Charge-insensitive qubit design derived from the cooper pair box, *Phys. Rev. A* **76**, 042319 (2007).
- [4] V. E. Manucharyan, J. Koch, L. I. Glazman, and M. H. Devoret, Fluxonium: Single Cooper-pair circuit free of charge offsets, *Science* **326**, 113 (2009).
- [5] L. B. Nguyen, Y.-H. Lin, A. Somoroff, R. Mencia, N. Grabon, and V. E. Manucharyan, High-coherence fluxonium qubit, *Phys. Rev. X* **9**, 041041 (2019).
- [6] A. Somoroff, Q. Ficheux, R. A. Mencia, H. Xiong, R. Kuzmin, and V. E. Manucharyan, Millisecond coherence in a superconducting qubit, *Phys. Rev. Lett.* **130**, 267001 (2023).
- [7] F. Wang, K. Lu, H. Zhan, L. Ma, F. Wu, H. Sun, H. Deng, Y. Bai, F. Bao, X. Chang, R. Gao, X. Gao, G. Gong, L. Hu, R. Hu, H. Ji, X. Ma, L. Mao, Z. Song, C. Tang, H. Wang, T. Wang, Z. Wang, T. Xia, H. Xu, Z. Zhan, G. Zhang, T. Zhou, M. Zhu, Q. Zhu, S. Zhu, X. Zhu, Y. Shi, H.-H. Zhao, and C. Deng, High-coherence fluxonium qubits manufactured with a wafer-scale-uniformity process, *Phys. Rev. Appl.* **23**, 044064 (2025).
- [8] Q. Ficheux, L. B. Nguyen, A. Somoroff, H. Xiong, K. N. Nesterov, M. G. Vavilov, and V. E. Manucharyan, Fast logic with slow qubits: Microwave-activated controlled-z gate on low-frequency fluxoniums, *Phys. Rev. X* **11**, 021026 (2021).
- [9] F. Bao, H. Deng, D. Ding, R. Gao, X. Gao, C. Huang, X. Jiang, H.-S. Ku, Z. Li, X. Ma, X. Ni, J. Qin, Z. Song, H. Sun, C. Tang, T. Wang, F. Wu, T. Xia, W. Yu, F. Zhang, G. Zhang, X. Zhang, J. Zhou, X. Zhu, Y. Shi, J. Chen, H.-H. Zhao, and C. Deng, Fluxonium: An alternative qubit platform for high-fidelity operations, *Phys. Rev. Lett.* **129**, 010502 (2022).
- [10] H. Xiong, Q. Ficheux, A. Somoroff, L. B. Nguyen, E. Dogan, D. Rosenstock, C. Wang, K. N. Nesterov, M. G. Vavilov, and V. E. Manucharyan, Arbitrary controlled-phase gate on fluxonium qubits using differential ac stark shifts, *Phys. Rev. Res.* **4**, 023040 (2022).
- [11] I. N. Moskalev, I. A. Simakov, N. N. Abramov, A. A. Grigorev, D. O. Moskalev, A. A. Pishchimova, N. S. Smirnov, E. V. Zikiy, I. A. Rodionov, and I. S. Besedin, High fidelity two-qubit gates on fluxoniums using a tunable coupler, *npj Quantum Inf.* **8**, 130 (2022).
- [12] E. Dogan, D. Rosenstock, L. Le Guevel, H. Xiong, R. A. Mencia, A. Somoroff, K. N. Nesterov, M. G. Vavilov, V. E. Manucharyan, and C. Wang, Two-fluxonium cross-resonance gate, *Phys. Rev. Appl.* **20**, 024011 (2023).
- [13] L. Ding, M. Hays, Y. Sung, B. Kannan, J. An, A. Di Paolo, A. H. Karamlou, T. M. Hazard, K. Azar, D. K. Kim, B. M. Niedzielski, A. Melville, M. E. Schwartz, J. L. Yoder, T. P. Orlando, S. Gustavsson, J. A. Grover, K. Serniak, and W. D. Oliver, High-fidelity, frequency-flexible two-qubit fluxonium gates with a transmon coupler, *Phys. Rev. X* **13**, 031035 (2023).
- [14] I. A. Simakov, G. S. Mazhorin, I. N. Moskalev, N. N. Abramov, A. A. Grigorev, D. O. Moskalev, A. A. Pishchimova, N. S. Smirnov, E. V. Zikiy, I. A. Rodionov, and I. S. Besedin, Coupler Microwave-Activated Controlled-Phase Gate on Fluxonium Qubits, *PRX Quantum* **4**, 040321 (2023).
- [15] X. Ma, G. Zhang, F. Wu, F. Bao, X. Chang, J. Chen, H. Deng, R. Gao, X. Gao, L. Hu, H. Ji, H.-S. Ku, K. Lu, L. Ma, L. Mao, Z. Song, H. Sun, C. Tang, F. Wang, H. Wang, T. Wang, T. Xia, M. Ying, H. Zhan, T. Zhou, M. Zhu, Q. Zhu, Y. Shi, H.-H. Zhao, and C. Deng, Native approach to controlled-z gates in inductively coupled fluxonium qubits, *Phys. Rev. Lett.* **132**, 060602 (2024).
- [16] H. Zhang, C. Ding, D. Weiss, Z. Huang, Y. Ma, C. Guinn, S. Sussman, S. P. Chitta, D. Chen, A. A. Houck, J. Koch, and D. I. Schuster, Tunable inductive coupler for high-fidelity gates between fluxonium qubits, *PRX Quantum* **5**, 020326 (2024).
- [17] W.-J. Lin, H. Cho, Y. Chen, M. G. Vavilov, C. Wang, and V. E. Manucharyan, 24 days-stable CNOT-gate on fluxonium qubits with over 99.9% fidelity, *PRX Quantum* **6**, 010349 (2025).
- [18] D. A. Rower, L. Ding, H. Zhang, M. Hays, J. An, P. M. Harrington, I. T. Rosen, J. M. Gertler, T. M. Hazard, B. M. Niedzielski, M. E. Schwartz, S. Gustavsson, K. Serniak, J. A. Grover, and W. D. Oliver, Suppressing Counter-Rotating Errors for Fast Single-Qubit Gates with Fluxonium, *PRX Quantum* **5**, 040342 (2024).
- [19] H. Sun, F. Wu, H.-S. Ku, X. Ma, J. Qin, Z. Song, T. Wang, G. Zhang, J. Zhou, Y. Shi, H.-H. Zhao, and C. Deng, Characterization of Loss Mechanisms in a Fluxonium Qubit, *Phys. Rev. Appl.* **20**, 034016 (2023).
- [20] P. Zhao, G. Zhao, S. Li, C. Zha, and M. Gong, Scalable fluxonium qubit architecture with tunable interactions between non-computational levels, [arXiv:2504.09888](https://arxiv.org/abs/2504.09888).
- [21] R. Barends and F. K. Wilhelm, Performance-centric roadmap for building a superconducting quantum computer, [arXiv:2506.23178](https://arxiv.org/abs/2506.23178).
- [22] A. Barenco, C. H. Bennett, R. Cleve, D. P. DiVincenzo, N. Margolus, P. Shor, T. Sleator, J. A. Smolin, and H. Weinfurter, Elementary gates for quantum computation, *Phys. Rev. A* **52**, 3457 (1995).
- [23] M. A. Nielsen and I. L. Chuang, Quantum Computation and Quantum Information (Cambridge University Press, Cambridge, 2000).
- [24] Y. Nam, Y. Su, and D. Maslov, Approximate quantum Fourier transform with $O(n \log(n))$ T gates, *npj Quantum Inf.* **6**, 26 (2020).
- [25] D. K. Park, F. Petruccione, and J.-K. K. Rhee, Circuit-based quantum random access memory for classical data, *Sci. Rep.* **9**, 3949 (2019).
- [26] K. M. Nakanishi, T. Satoh, and S. Todo, Decompositions of multiple controlled-Z gates on various qubit-coupling graphs, *Phys. Rev. A* **110**, 012604 (2024).
- [27] A. Mandviwalla, K. Ohshiro, and B. Ji, Implementing Grover's Algorithm on the IBM Quantum Computers, in *Proceedings of the 2018 IEEE International Conference on Big Data (Big Data) (IEEE, 2018)*, pp. 2531-2537.
- [28] Z. Liang, Z. Wang, J. Yang, L. Yang, Y. Shi, and W. Jiang, Can noise on qubits be learned in quantum neural network? a case study on quantumflow, in *2021 IEEE/ACM International Conference On Computer Aided Design (ICCAD)*, (IEEE, 2021), pp. 1-7.
- [29] K. Bharti, A. Cervera-Lierta, T. H. Kyaw, T. Haug, S. Alperin-Lea, A. Anand, M. Degroote, H. Heimonen, J. S. Kottmann, T. Menke, W.-K. Mok, S. Sim, L.-C. Kwek, and A. Aspuru-Guzik, Noisy intermediate-scale quantum algorithms, *Rev. Mod. Phys.*

- 94**, 015004 (2022).
- [30] A. Paetznick and B. W. Reichardt, Universal Fault-Tolerant Quantum Computation with Only Transversal Gates and Error Correction, *Phys. Rev. Lett.* **111**, 090505 (2013).
- [31] T. J. Yoder, R. Takagi, and I. L. Chuang, Universal Fault Tolerant Gates on Concatenated Stabilizer Codes, *Phys. Rev. X* **6**, 031039 (2016).
- [32] R. Chao and B. W. Reichardt, Fault-tolerant quantum computation with few qubits, *npj Quantum Inf.* **4**, 42 (2018).
- [33] S. Tasler, J. Old, L. Heunisch, V. Feulner, T. Eckstein, M. Müller, and M. J. Hartmann, Optimizing Superconducting Three-Qubit Gates for Surface-Code Error Correction, [arXiv:2506.09028](https://arxiv.org/abs/2506.09028).
- [34] J. Old, S. Tasler, M. J. Hartmann, and M. Müller, Fault-Tolerant Stabilizer Measurements in Surface Codes with Three-Qubit Gates, [arXiv:2506.09029](https://arxiv.org/abs/2506.09029).
- [35] E. Zahedinejad, J. Ghosh, and B. C. Sanders, High-Fidelity Single-Shot Toffoli Gate via Quantum Control, *Phys. Rev. Lett.* **114**, 200502 (2015).
- [36] E. Zahedinejad, J. Ghosh, and B. C. Sanders, Designing High-Fidelity Single-Shot Three-Qubit Gates: A Machine-Learning Approach, *Phys. Rev. Appl.* **6**, 054005 (2016).
- [37] E. Barnes, C. Arenz, A. Pitchford, and S. E. Economou, Fast microwave-driven three-qubit gates for cavity-coupled superconducting qubits, *Phys. Rev. B* **96**, 024504 (2017).
- [38] S. P. Pedersen, K. S. Christensen, and N. T. Zinner, Native three-body interaction in superconducting circuits, *Phys. Rev. Res.* **1**, 033123 (2019).
- [39] M. Khazali and K. Mølmer, Fast Multiqubit Gates by Adiabatic Evolution in Interacting Excited-State Manifolds of Rydberg Atoms and Superconducting Circuits, *Phys. Rev. X* **10**, 021054 (2020).
- [40] W. Feng and D.-W. Wang, Quantum Fredkin gate based on synthetic three-body interactions in superconducting circuits, *Phys. Rev. A* **101**, 062312 (2020).
- [41] P. Zhao, P. Xu, D. Lan, X. Tan, H. Yu, and Y. Yu, Switchable Next-Nearest-Neighbor Coupling for Controlled Two-Qubit Operations, *Phys. Rev. Appl.* **14**, 064016 (2020).
- [42] S. E. Rasmussen, K. Groenland, R. Gerritsma, K. Schoutens, and N. T. Zinner, Single-step implementation of high-fidelity n -bit Toffoli gates, *Phys. Rev. A* **101**, 022308 (2020).
- [43] S. E. Rasmussen and N. T. Zinner, Simple implementation of high fidelity controlled-iSWAP gates and quantum circuit exponentiation of non-Hermitian gates, *Phys. Rev. Res.* **2**, 033097 (2020).
- [44] X. Gu, J. Fernández-Pendás, A. Bengtsson, P. Vikstål, T. Abad, C. Warren, G. Tancredi, V. Shumeiko, G. Johansson, and A. Frisk Kockum, Fast Multiqubit Gates through Simultaneous Two-Qubit Gates, *PRX Quantum* **2**, 040348 (2021).
- [45] A. J. Baker, G. B. P. Huber, N. J. Glaser, F. Roy, I. Tsitsilin, S. Filipp, and M. J. Hartmann, Single shot i -Toffoli gate in dispersively coupled superconducting qubits, *Appl. Phys. Lett.* **120**, 054002 (2022).
- [46] N. J. Glaser, F. Roy, and S. Filipp, Controlled-Controlled-Phase Gates for Superconducting Qubits Mediated by a Shared Tunable Coupler, *Phys. Rev. Appl.* **19**, 044001 (2023).
- [47] I. A. Simakov, G.S. Mazhorin, I. N. Moskalenko, S. S. Seidov, and I. S. Besedin, High-fidelity transmon-coupler-activated CCZ gate on fluxonium qubits, *Phys. Rev. Appl.* **21**, 044035 (2024).
- [48] K. Zhao, W.-G. Ma, Z. Wang, H. Li, K. Huang, Y.-H. Shi, K. Xu, and H. Fan, A microwave-activated high-fidelity three-qubit gate scheme for fixed-frequency superconducting qubits, [arXiv:2504.21346](https://arxiv.org/abs/2504.21346).
- [49] C. Song, S.-B. Zheng, P. Zhang, K. Xu, L. Zhang, Q. Guo, W. Liu, D. Xu, H. Deng, K. Huang, D. Zheng, X. Zhu, and H. Wang, Continuous-variable geometric phase and its manipulation for quantum computation in a superconducting circuit, *Nat. Commun.* **8**, 1061 (2017).
- [50] S. Li, J. Clark, S. Wang, Y. Wu, M. Gong, Z. Yan, H. Rong, H. Deng, C. Zha, C. Guo, L. Sun, C. Peng, X. Zhu, and J.-W. Pan, Realisation of high-fidelity nonadiabatic CZ gates with superconducting qubits, *npj Quantum Inf.* **5**, 84 (2019).
- [51] T. Roy, S. Hazra, S. Kundu, M. Chand, M. P. Patankar, and R. Vijay, Programmable Superconducting Processor with Native Three-Qubit Gates, *Phys. Rev. Appl.* **14**, 014072 (2020).
- [52] Y. Kim, A. Morvan, L. B. Nguyen, R. K. Naik, C. Jünger, L. Chen, J. M. Kreikebaum, D. I. Santiago, and I. Siddiqi, High-fidelity three-qubit i Toffoli gate for fixed-frequency superconducting qubits, *Nat. Phys.* **18**, 783 (2022).
- [53] C. W. Warren, J. Fernández-Pendás, S. Ahmed, T. Abad, A. Bengtsson, J. Biznárová, K. Debnath, X. Gu, C. Krizán, A. Osman, A. F. Roudsari, P. Delsing, G. Johansson, A. F. Kockum, G. Tancredi, and J. Bylander, Extensive characterization and implementation of a family of three-qubit gates at the coherence limit, *npj Quantum Inf.* **9**, 44 (2023).
- [54] C. K. Hu, J. Yuan, B. A. Veloso, J. Qiu, Y. Zhou, L. Zhang, J. Chu, O. Nurbolat, L. Hu, J. Li, Y. Xu, Y. Zhong, S. Liu, F. Yan, D. Tan, R. Bachelard, A. C. Santos, C. Villas-Boas, and D. Yu, Native conditional i SWAP operation with superconducting artificial atoms, *Phys. Rev. Appl.* **20**, 034072 (2023).
- [55] T. Itoko, M. Malekakhlagh, N. Kanazawa, and M. Takita, Three-qubit parity gate via simultaneous cross-resonance drives, *Phys. Rev. Appl.* **21**, 034018 (2024).
- [56] H.-T. Liu, B.-J. Chen, J.-C. Zhang, Y.-X. Xiao, T.-M. Li, K. Huang, Z. Wang, H. Li, K. Zhao, Y. Xu, C.-L. Deng, G.-H. Liang, Z.-H. Liu, S.-Y. Zhou, C.-P. Fang, X. Song, Z. Xiang, D. Zheng, Y.-H. Shi, K. Xu, and H. Fan, Direct Implementation of High-Fidelity Three-Qubit Gates for Superconducting Processor with Tunable Couplers, [arXiv:2501.18319](https://arxiv.org/abs/2501.18319).
- [57] C. Miao, S. Léger, Z. Li, G. Lee, L. Jiang, and D. I. Schuster, Implementation of a quantum addressable router using superconducting qubits, [arXiv:2503.04295](https://arxiv.org/abs/2503.04295).
- [58] A. Mezzacapo, L. Lamata, S. Filipp, and E. Solano, Many-Body Interactions with Tunable-Coupling Transmon Qubits, *Phys. Rev. Lett.* **113**, 050501 (2014).
- [59] P. Zhao, X. Tan, H. Yu, S.-L. Zhu, and Yang Yu, Circuit QED with qutrits: Coupling three or more atoms via virtual-photon exchange, *Phys. Rev. A* **96**, 043833 (2017).
- [60] M. Sameti, A. Potočnik, D. E. Browne, A. Wallraff, and M. J. Hartmann, Superconducting quantum simulator for topological order and the toric code, *Phys. Rev. A* **95**, 042330 (2017).
- [61] J. H. Busnaina, Z. Shi, J. M. Alcaine-Cuervo, C. X. C. Yang, I. Nsanzineza, E. Rico, and C.M. Wilson, Native Three-Body Interactions in a Superconducting Lattice Gauge Quantum Simulator, [arXiv:2501.13383](https://arxiv.org/abs/2501.13383).
- [62] X. You, J. A. Sauls, and J Koch, Circuit quantization in the presence of time-dependent external flux, *Phys. Rev. B* **99**, 174512 (2019).
- [63] J. M. Chow, J. M. Gambetta, A. W. Cross, S. T. Merkel, C. Rigetti, and M. Steffen, Microwave-activated conditional-phase gate for superconducting qubits, *New J. Phys.* **15**, 115012 (2013).
- [64] K. N. Nesterov, I. V. Pechenezhskiy, C. Wang, V. E. Manucharyan, and M. G. Vavilov, Microwave-activated controlled- z gate for fixed-frequency fluxonium qubits, *Phys. Rev. A* **98**, 030301 (2018).
- [65] M. H. Goerz, F. Motzoi, K. B. Whaley, and C. P. Koch, Charting

- the circuit QED design landscape using optimal control theory, *npj Quantum Inf.* **3**, 37 (2017).
- [66] Y. Sung, L. Ding, J. Braumüller, A. Vepsäläinen, B. Kannan, M. Kjaergaard, A. Greene, G. O. Samach, C. McNally, D. Kim, A. Melville, B. M. Niedzielski, M. E. Schwartz, J. L. Yoder, T. P. Orlando, S. Gustavsson, and W. D. Oliver, Realization of High-Fidelity CZ and ZZ-Free iSWAP Gates with a Tunable Coupler, *Phys. Rev. X* **11**, 021058 (2021).
- [67] P. Zhao, D. Lan, P. Xu, G. Xue, M. Blank, X. Tan, H. Yu, and Y. Yu, Suppression of Static ZZ Interaction in an All-Transmon Quantum Processor, *Phys. Rev. Appl.* **16**, 024037 (2021).
- [68] F. Motzoi, J. M. Gambetta, P. Rebentrost, and F. K. Wilhelm, Simple Pulses for Elimination of Leakage in Weakly Nonlinear Qubits, *Phys. Rev. Lett.* **103**, 110501 (2009).
- [69] C. J. Wood and J. M. Gambetta, Quantification and characterization of leakage errors, *Phys. Rev. A* **97**, 032306 (2018).
- [70] L. H. Pedersen, N. M. Møller, and K. Mølmer, Fidelity of quantum operations, *Phys. Lett. A* **367**, 47 (2007).
- [71] This can be made more explicit by comparing CCZ gate errors with different pulse shapes shown in Fig. 3(a). One can find that the flat-top cosine pulse achieves the lowest infidelity among the three pulse shapes (Cosine, Gaussian, and Flat-top cosine), attributable to its reduced drive amplitude. Reducing drive amplitude mitigates the ac-Stark shifts, thereby diminishing the resulting accumulated multi-qubit phases. This effect is analogous to the phase accumulation discussed in microwave-driven two-fluxonium systems, see, e.g., Refs. [10, 13].
- [72] M. Khezri, Dispersive measurement of superconducting qubits (University of California, Riverside, 2018).
- [73] D. Zueco, G. M. Reuther, S. Kohler, and P. Hänggi, Qubit-oscillator dynamics in the dispersive regime: Analytical theory beyond the rotating-wave approximation, *Phys. Rev. A* **80**, 033846 (2009).
- [74] F. Yan, P. Krantz, Y. Sung, M. Kjaergaard, D. L. Campbell, T. P. Orlando, S. Gustavsson, and W. D. Oliver, Tunable Coupling Scheme for Implementing High-Fidelity Two-Qubit Gates, *Phys. Rev. Appl.* **10**, 054062 (2018).
- [75] E. L. Rosenfeld, C. T. Hann, D. I. Schuster, M. H. Matheny, and A. A. Clerk, High-Fidelity Two-Qubit Gates between Fluxonium Qubits with a Resonator Coupler, *PRX Quantum* **5**, 040317 (2024).
- [76] J. Johansson, P. Nation, and F. Nori, QuTiP: An open-source Python framework for the dynamics of open quantum systems, *Comput. Phys. Commun.* **183**, 1760 (2012).
- [77] T. Abad, A. F. Kockum, and G. Johansson, Impact of decoherence on the delity of quantum gates leaving the computational subspace, [arXiv:2302.13885](https://arxiv.org/abs/2302.13885).